

Proposed two-dimensional topological insulator in SiTe

Yandong Ma,^{1,2,*} Liangzhi Kou,³ Ying Dai,⁴ and Thomas Heine^{1,2,†}

¹*Wilhelm-Ostwald-Institut für Physikalische und Theoretische Chemie, Universität Leipzig, Linnéstr. 2, 04103 Leipzig, Germany*

²*Department of Physics and Earth Sciences, Jacobs University Bremen, Campus Ring 1, 28759 Bremen, Germany*

³*School of Chemistry, Physics and Mechanical Engineering Faculty, Queensland University of Technology, Garden Point Campus, QLD 4001, Brisbane, Australia*

⁴*School of Physics, Shandong University, Shandan Str. 27, 250100 Jinan, People's Republic of China*

(Received 11 July 2016; revised manuscript received 24 October 2016; published 9 November 2016)

The two-dimensional (2D) crystal SiTe is identified to be a 2D topological insulator (TI) with bulk band gap of 220 meV by means of first-principles calculations. The synthesis of 2D SiTe has been reported earlier [Phys. Status Solidi RRL **8**, 302 (2014)] as part of a three-dimensional superlattice. The freestanding monolayer is thermally and dynamically stable and only weakly bound within the layered superlattice, offering the possibility of mechanical exfoliation. Our discovery of a topological signature with large band gap raises the expectation that the most apparent showstopper in experimental 2D TI research, the lack of stable materials exposing a quantum spin Hall effect at room temperature, can be overcome. This offers many laboratories an opportunity to participate in investigating exciting new phenomena in condensed matter physics, such as new quasiparticles and dissipationless spin transport.

DOI: [10.1103/PhysRevB.94.201104](https://doi.org/10.1103/PhysRevB.94.201104)

Two-dimensional (2D) topological insulators (TIs), also known as quantum spin Hall (QSH) insulators, are new states of quantum matter characterized by the conducting edge states inside the bulk gap as protected by time-reversal symmetry [1,2]. Charge carriers in such edge states are helical Dirac fermions, which are immune to nonmagnetic scattering and exhibit dissipationless transport. Hence, they are expected to lead to fascinating applications in energy-efficient electronic devices and spintronics [3]. So far, experimental verifications of 2D TIs in real systems are limited to the HgTe/CdTe [4] and InAs/GaSb [5] quantum wells. Moreover, extreme conditions, e.g., precisely controlled molecular-beam epitaxy and ultralow temperature (due to their small bulk gap of the order of meV), are required in experiment, thus greatly obstructing the exploitation and application of the QSH effect. Besides, recently, there are also some experimental attempts to observe the QSH effect in experiments [6–8]. Therefore, there is a great interest in searching for suitable 2D TI materials with sizable band gaps and characteristics of easy fabrication. Recently, a variety of 2D materials have been predicted to harbor the 2D TI phase, such as oxygen functionalized MXene [9], arsenene [10], Ni₃C₁₂S₁₂ monolayer [11], 2D transition-metal halide [12], 2D transition-metal dichalcogenides [13–15], III-Bi monolayers [16], TiS_{2-x}Te_x monolayers [17], Bi bilayer [18], BiF thin film [19], functionalized Bi/Sb monolayers [20–22], Bi₄Br₄ 2D crystals [23], ZrTe₅/HfTe₅ 2D crystals [24], functionalized Ge/Sn thin films [25–27], and modified phosphorene [28]. Unfortunately, most of these theoretically proposed structures do not exist in nature and remain to be created in experiments.

Among these systems, the Bi₄Br₄ and ZrTe₅/HfTe₅ 2D crystals seem to be very promising because they could be cleaved from the experimentally existing three-dimensional (3D) layered materials and their nontrivial

gaps are sizable, although their atomic structures might be too complicated. IV-VI 2D materials are also known to hold great potential for the investigation of nontrivial topological properties and there are several theoretical proposals available in literature, e.g., 2D topological crystalline insulators in rocksalt 2D crystals [29–32]. However, these hypothetical rocksalt IV-VI 2D structures suffer from structural instability and high surface chemical activity and have yet to be synthesized in experiments. Recently, hexagonal IV-VI (SiTe, GeTe) 2D building blocks with a simple atomic structure were experimentally confirmed in IV-VI/Sb₂Te₃ superlattices in which the VI-IV-IV-VI and Te-Sb-Te-Sb-Te layers are connected by van der Waals (vdW) interactions [33–35]. Interestingly, these sandwich-type superlattices are phase change materials with a great potential as interfacial phase change memory [33,34]. Meanwhile, another configuration of silicon telluride, with a layered structure, has caught the attention of the 2D electronics community [36]. The progress in understanding this material class in recent experiments, as well as the presence of only weak interlayer interactions, suggests that the hexagonal SiTe and GeTe 2D crystals can be obtained by mechanical exfoliation techniques from their layered vdW superlattice crystals akin to fabricating graphene from graphite.

Here, on the basis of density functional theory (DFT), we demonstrate that the SiTe 2D crystal with a hexagonal structure is a 2D TI with a sizable bulk band gap of 0.220 eV, without any additional tuning. The calculated Z_2 invariant and helical metallic edge states provide direct evidence for its nontrivial topological properties. This sizable-gap 2D TI is an ideal candidate for experimental studies on the QSH effect because it has a simple stoichiometric ratio and crystal structure, and most importantly, it can be naturally obtained by cleaving from its experimentally existing superlattice. The phonon spectrum calculations and *ab initio* molecular dynamics (MD) simulations confirm that this 2D crystal is dynamically and thermally stable. Moreover, a precise control of its topological state can be achieved by applying strain. Our

*Corresponding author: myd1987@gmail.com

†Corresponding author: thomas.heine@uni-leipzig.de

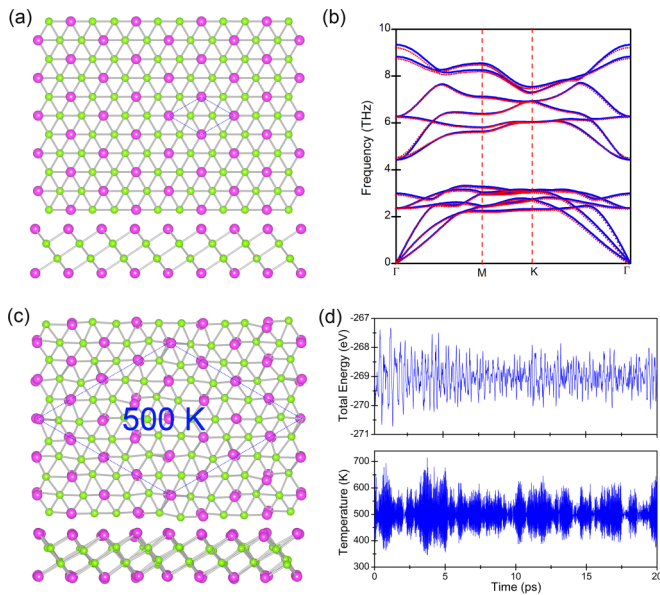


FIG. 1. (a) Top and side views of the atomic structure of SiTe 2D crystal, with the dashed line marking the unit cell. (b) Phonon spectra of SiTe 2D crystal calculated with (red) and without (blue) SOC. (c) Top and side views of the snapshot of SiTe 2D crystal at the end of MD simulation at 500 K; the dashed line indicates the supercell used in the simulation. (d) Changes of temperature and energy with time obtained from MD simulation of SiTe 2D crystal at 500 K. The green and pink balls represent Si and Te atoms, respectively.

work thus represents the discovery of a 2D TI signature in an existing material, possibly the breakthrough in realizing 2D TI research in the laboratory.

First-principles calculations based on DFT are carried out by using the projector augmented wave method as implemented in the plane-wave code VASP [37–39]. For structural relaxations and band-structure calculations, generalized gradient approximation with Perdew-Burke-Ernzerhof (PBE) parametrization [40] is employed. To overcome the problem of band-gap underestimation in semilocal exchange-correlation functionals, the Heyd-Scuseria-Ernzerhof (HSE06) hybrid functional [41] is also used for calculating the band structures. If not specified, the results are based on PBE. A cutoff energy of 500 eV is used throughout all calculations. Structures are fully relaxed until residual forces on each atom are less than 0.01 eV/Å. Brillouin zone (BZ) integration is performed with the k -point meshes [42] of $15 \times 15 \times 1$. The vacuum space is 20 Å to ensure that interactions between layers are negligible. Spin-orbit coupling (SOC) is included at the second variational step using scalar-relativistic eigenfunctions as a basis. The phonon calculations are carried out using the PHONOPY program which relies on density functional perturbation theory [43,44]. The *ab initio* MD simulations are performed by adopting the canonical ensemble with a Nosé thermostat.

The optimized structure of SiTe 2D crystal is shown in Fig. 1(a). This structure possesses a hexagonal Bravais lattice and a $P-3m1$ symmetry with an inversion center located at the center of two nonequivalent Si atoms. Within each unit cell [marked by the dashed line in Fig. 1(a)], it contains two 6-coordinated Si atoms and two 3-coordinated Te atoms. The surfaces of SiTe 2D crystal are basically terminated by the

3-coordinated Te atoms, as is the case in the Bi_2Te_3 family, and thus they are chemically inert. In fact, by replacing the internal Bi-Te-Bi layer with the Si-Si layer in the Bi_2Te_3 sheet, the geometry of the SiTe 2D crystal can be realized. For more details about the structure (please see Supplemental Material [45]). Both the stoichiometric ratio and crystal structure of SiTe 2D crystal are relatively simple, which would be beneficial to its mechanical exfoliation from the layered superlattice and further applications.

The structural stability of SiTe 2D crystal is first examined by analyzing its phonon spectrum. The phonon band dispersion curves are shown in Fig. 1(b). It can be clearly seen that the obtained phonon dispersions without (blue lines) and with (red lines) considering SOC agree well with each other: all the branches have positive frequencies without any imaginary phonon modes in the entire BZ, thus confirming the dynamic stability of this 2D crystal. The thermal stability of SiTe 2D crystal is further investigated by performing *ab initio* MD simulations. To approach the true stability, we adopt a relatively large supercell consisting of 4×4 repeated unit cells [marked by a dashed line in Fig. 1(c)] to simulate the 2D lattice. After heating at 300 and 500 K for 20 ps with a time step of 1 fs, we find no structure reconstruction in either of the cases, suggesting that SiTe 2D crystal is thermally stable. The snapshots of atomic configurations of SiTe 2D crystal at the end of MD simulations at 500 and 300 K are presented in Fig. 1(c) and Fig. S1(a) [45], respectively, and the corresponding fluctuations of energy and temperature with time during the simulations are shown in Fig. 1(d) and Fig. S1(b) [45]. Our stability analysis predicts single-layer SiTe to be intrinsically stable, and it suggests that there is a high probability that the SiTe layer can be exfoliated from its superlattice, following common exfoliation techniques [46].

The PBE band structures of SiTe 2D crystal without and with SOC are shown in Fig. 2(a). In the vicinity of Fermi level, the valence and conduction bands are mainly contributed by Si/Te $-p_{x,y}$ orbitals. Without including SOC, the valence and conduction bands of SiTe 2D crystal exhibit a parabolic character and the valence band maximum (VBM) and conduction band minimum (CBM) degenerate at Γ point with Fermi level locating exactly at the degenerate point. The 3D plot of band dispersions of SiTe 2D crystal around Fermi level is shown in Fig. 2(c). Thus, in the absence of SOC, SiTe 2D crystal is a gapless semiconductor. After turning on SOC, the degenerate point is lifted and Fermi level separates the valence and conduction bands, leading to a sizable global band gap of 129 meV, as shown in Fig. 2(a); and this band gap is related to the strong SOC strength within $p_{x,y}$ orbitals, which is similar to cases of functionalized Ge/Sn thin films [25–27]. SiTe 2D crystal thus becomes an insulator under SOC. Such a SOC-induced transition from a gapless semiconductor to an insulator strongly suggests that SiTe 2D crystal is a 2D TI [12,19–22,27]. We will confirm this hypothesis below.

Since PBE usually underestimates the band gap, we adopt hybrid functional HSE06 to get a more precise description of the band structures of SiTe 2D crystal, and the corresponding results are plotted in Fig. 2(b). The SOC-induced indirect band gap calculated by using HSE06 is found to be 220 meV, significantly larger than the PBE result (129 meV), while the

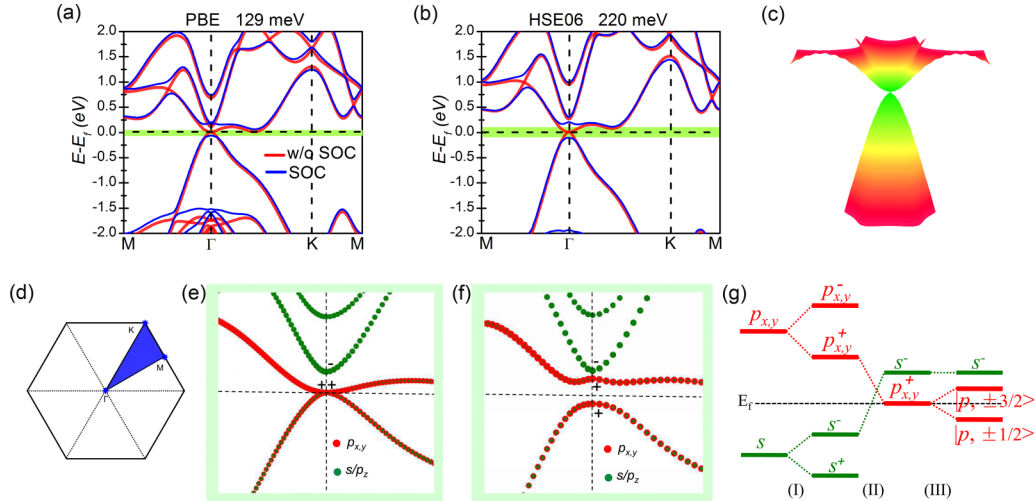


FIG. 2. Electronic structures of SiTe 2D crystal without and with SOC calculated by using (a) PBE and (b) HSE06 potentials. (c) Band dispersions of SiTe 2D crystal around Fermi level in 2D k space with energy as the third dimension. (d) 2D Brillouin zone of SiTe 2D crystal. Orbital-resolved band dispersions near Fermi level for SiTe 2D crystal (e) without and (f) with SOC calculated by using HSE06 potential; parities of bands at the Γ point are labeled by “+” and “-.” (g) Schematic diagram of the evolution of energy levels at the Γ point for SiTe 2D crystal under (I) chemical bonding, (II) crystal field effect, and (III) SOC in sequence.

band structure without introducing the SOC gap has the same characteristics as in the PBE calculation, whereas the SOC strength, defined as SOC-induced splitting of the degenerate bands at Γ point, calculated by using PBE (271 meV) and HSE06 (310 meV) are close. It is worthy to notice that the band structure of SiTe 2D crystal under SOC in consideration is a little special: the CBM locates almost at the center between the Γ and K points instead of in the vicinity of the Γ point. From Figs. 2(a) and 2(b), it can be clearly seen that the VBM calculated by using HSE06 shifts a little further away from Fermi level as compared with that based on PBE. Therefore, although the difference between SOC strength based on PBE and HSE06 is relatively small, the calculated global band gap based on HSE06 is significantly larger than that predicted by PBE. Despite the difference in band gap, the main characters of the PBE and HSE06 band structures are roughly similar to each other, regardless if SOC is included or not.

To verify the nontrivial band topology of SiTe 2D crystal, we investigate the topological Z_2 invariant following the parity criterion proposed by Fu *et al.* [47]. The parities are calculated for each pair of Kramers’ degenerate occupied bands at all time-reversal invariant momenta points in the 2D Brillouin zone [see Fig. 2(d)], one Γ and three M points. The results indicate that SiTe 2D crystal indeed is a 2D TI with $Z_2 = 1$ (see Supplemental Material Table S1 [45]). Considering its sizable nontrivial gap of 220 meV, the QSH effect can be readily observed in SiTe 2D crystal at room temperature. The physical manifestation of a nontrivial topological invariant is the existence of conducting edge states that are protected by the time-reversal symmetry. To simulate the topological edge states of SiTe 2D crystal, we construct two types of SiTe nanoribbons by cutting the 2D lattices along different directions. The width of SiTe nanoribbons with zigzag and linear (from the top view) edges are selected to be 89.7 and 89.3 Å, respectively, to avoid spurious interactions between the two edges. Figure 3 shows their crystal and band structures. Because each nanoribbon has two symmetric

edges (highlighted in green and pink), the edge states from two sides are degenerate in energy. For the nanoribbon with zigzag edges, as shown in Fig. 3(a), the conducting edge states appear in the band gap and cross linearly with each other at the $\bar{\Gamma}$ point. For the nanoribbon with linear edges, although the detailed band dispersions of edge states are different from that with zigzag edges, there are still gapless edge states crossing linearly in the band gap at the $\bar{\Gamma}$ point [see Fig. 3(c)]. If the shape of the edges is changed, modifications of the Hamiltonian near the edges would be required, and thus the dispersion of the edge states would be modified [48,49]. However, the existence of the edge states is determined by the topological structure of the bulk states, which is summarized by the bulk-boundary correspondence [48,49]. Therefore, if the nontrivial band topology is protected, the conducting edge states always exist, but their detailed form may depend on the shape of the edge. These results also confirm the 2D TI state in SiTe 2D crystal.

Figures 2(e) and 2(f) show the orbital-resolved band dispersions of SiTe 2D crystal near Fermi level without and with SOC, respectively. Obviously, no band inversion can be observed and thus the nontrivial band order in SiTe 2D crystal is not due to the effect of SOC. To uncover the underlying mechanism of the band inversion and topology nature of SiTe 2D crystal, we analyze the orbital evolution at Γ point in detail and the result is shown in Fig. 2(g). Since the states around Fermi level are dominated by s and $p_{x,y}$ orbitals, here we focus on these orbitals and ignore the other ones. We start from the isolated atomic orbitals and consider the effect of (I) chemical bonding, (II) crystal field, and (III) SOC in sequence. At stage (I), atomic orbitals hybridize to form bonding and antibonding states, which are labeled as $|s^\pm\rangle$ and $|p_{x,y}^\pm\rangle$ (superscripts \pm represent parities of states). Among them, as shown in Fig. 2(g), $|s^-\rangle$ and $|p_{x,y}^+\rangle$ are close to Fermi level, with $|s^-\rangle$ locating below $|p_{x,y}^+\rangle$. Here the model under chemical bonding effect is simulated by stretching the lattice constant from a to $1.5a$. When crystal field effect is taken into

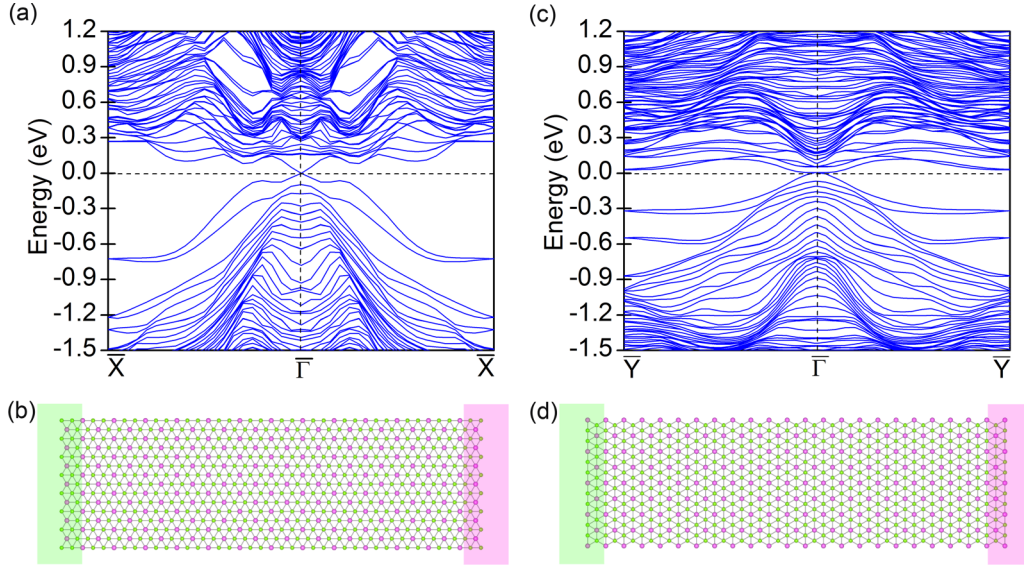


FIG. 3. Electronic band structures and corresponding crystal structures for SiTe nanoribbon with [(a),(b)] zigzag and [(c),(d)] linear edges. The left and right edges of each nanoribbon are highlighted in green and pink, respectively.

account in stage (II), namely, compressing the structure to the equivalent position, band inversion occurs between $|s^- \rangle$ and $|p_{x,y}^+ \rangle$, leading to a nontrivial band order in SiTe 2D crystal. In the inverted band structure, $|s^- \rangle$ is unoccupied and degenerate $|p_{x,y}^+ \rangle$ is half occupied, thereby the systems become a gapless semiconductor. After further introducing SOC in stage (III), the degeneracy of the half-occupied $|p_{x,y}^+ \rangle$ is lifted and an energy gap is created. During this stage, no parity exchange between occupied and unoccupied states is observed, that is, the inverted band order remains unchanged. Consequently, the band inversion in SiTe 2D crystal stems from crystal field effect instead of SOC, and the effect of SOC is to create an energy gap. It is interesting to note that the s - p band inversion in SiTe 2D crystal is different from the conventional s - p band inversion where $|s^- \rangle$ is typically occupied in the inverted band order [25–27].

In what follows, we investigate the effect of external strain on the topological properties of SiTe 2D crystal. The strain range considered here is from -6% to 6% . It should be noted that the simulations under strong compressive strain are about academic interest rather than for practical applications due to

difficulties in experimental realization. Figure 4(b) shows the relative positions of the $|s^- \rangle$ and $|p_{x,y}^+ \rangle$ states at the Γ point and the global band gap (E_g) of SiTe 2D crystal as a function of strain calculated by using HSE06; Fig. S2 [45] shows the corresponding band structures under various strains. Within the strain range from -2% to 2% , the band topology of SiTe 2D crystal remains nontrivial, which is identified by the topological Z_2 invariant. And the corresponding nontrivial band gap increases from 110 to 239 meV and then decreases to 90 meV with increasing strain from -2% to 2% . When decreasing the compressive strain by more than -3% , although $|s^- \rangle$ still lies above the upper $|p_{x,y}^+ \rangle$, the absence of a global band gap suggests that SiTe 2D crystal transforms into a metal. On the other hand, by increasing the stretch strain to 3% , as shown in Fig. 4(b), $|s^- \rangle$ shifts below the lower $|p_{x,y}^+ \rangle$, yielding to a parity exchange between the unoccupied and occupied bands at the Γ point, and in turn, inducing a topological phase transition from nontrivial phase to trivial phase. It will be very interesting to observe such topological phase transition experimentally, simply by stretching the sample. For the result calculated by using PBE, as shown in Fig. 4(a) and Fig. S3

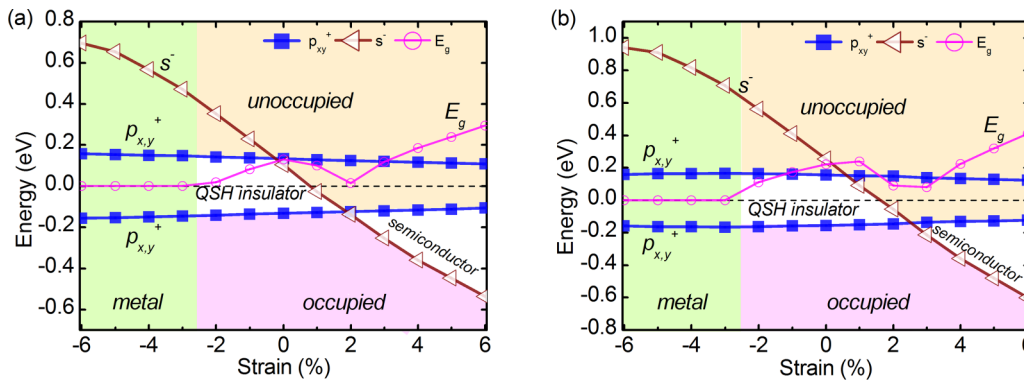


FIG. 4. The relative positions of $|s^- \rangle$ and $|p_{x,y}^+ \rangle$ states at the Γ point and the global band gap (E_g) of SiTe 2D crystal as a function of strain calculated by using (a) PBE and (b) HSE06 potentials. When $|s^- \rangle$ lies below $|p_{x,y}^+ \rangle$, the band topology is trivial.

[45], it shares a similar trend with that of HSE06, but with a slight difference in critical strains and global band gaps.

Furthermore, we extended our study to hexagonal GeTe and SnTe 2D crystals, which are isoelectronic counterparts of SiTe 2D crystal. It should be noted that these structures are different from the previously studied configurations [29–32]. Figure S4 [45] plots their PBE and HSE06 band structures without and with SOC. We find that, different from SiTe 2D crystals, both GeTe and SnTe 2D crystals turn out to be trivial semiconductors with an indirect band gap. To see whether it is from the changes of their crystal structures, we calculate the band structures of GeTe and SnTe 2D crystals by employing the crystal structure of SiTe 2D crystal without any further relaxation: under this condition, GeTe 2D crystal is still a trivial semiconductor [see Figs. S5(a) and S5(b) [45]], while SnTe 2D crystal becomes a 2D TI with a nontrivial topological invariant [see Figs. S5(c) and S5(d) [45]]. Clearly, the absence of topological phases in GeTe and SnTe 2D crystals stems not only from the changes of structures but also from the difference in the intrinsic properties of atoms (such as electronegativity, radii).

In summary, using first-principles calculations, we identify that SiTe 2D crystal with simple stoichiometric ratio and crystal structure is an ideal 2D TI, presenting a sizable nontrivial gap of 0.220 eV. The mechanism for its nontrivial band topology is from the band inversion between $|s^- \rangle$ and $|p_{x,y}^+ \rangle$ states induced by crystal field effect. This material is dynamically and thermally stable. Remarkably, different from most of the previous proposed 2D TIs where the materials do not naturally exist and remain to be synthesized, 2D SiTe can be obtained by cleaving from its experimentally available superlattice. Besides, a precise control of its band topology can be achieved by applying strain. Considering these merits, we envision that the QSH effect can be observed experimentally in SiTe 2D crystal soon, which will greatly advance the practical applications of 2D TIs.

Financial support by the Deutsche Forschungsgemeinschaft (DFG, Grant No. HE 3543/18-1) and the National Science Foundation of China under Grant No. 11174180 are gratefully acknowledged. We thank ZIH Dresden for computer time. The authors declare no competing financial interests.

-
- [1] B. A. Bernevig, T. L. Hughes, and S.-C. Zhang, Quantum spin Hall effect and topological phase transition in HgTe quantum wells, *Science* **314**, 1757 (2006).
- [2] N. Nagaosa, A new state of quantum matter, *Science* **318**, 758 (2007).
- [3] A. Roth, C. Brune, H. Buhmann, L. W. Molenkamp, J. Maciejko, X.-L. Qi, and S.-C. Zhang, Nonlocal transport in the quantum spin Hall state, *Science* **325**, 294 (2009).
- [4] M. König, S. Wiedmann, C. Brüne, A. Roth, H. Buhmann, L. W. Molenkamp, X. L. Qi, and S. C. Zhang, Quantum spin Hall insulator state in HgTe quantum wells, *Science* **318**, 766 (2007).
- [5] I. Knez, R. R. Du, and G. Sullivan, Evidence for Helical Edge Modes in Inverted InAs/GaSb Quantum Wells, *Phys. Rev. Lett.* **107**, 136603 (2011).
- [6] S. H. Kim, K.-Y. Jin, J. Park, J. S. Kim, S. H. Jhi, T. H. Kim, and H. W. Yeom, Edge and interfacial states in a two-dimensional topological insulator: Bi(111) bilayer on Bi₂Te₂Se, *Phys. Rev. B* **89**, 155436 (2014).
- [7] S. H. Kim, K.-Y. Jin, J. Park, J. S. Kim, S. H. Jhi, and H. W. Yeom, Topological phase transition and quantum spin Hall edge states of antimony few layers, [arXiv:1604.02940](https://arxiv.org/abs/1604.02940).
- [8] R. Wu, J.-Z. Ma, S.-M. Nie, L.-X. Zhao, X. Huang, J.-X. Yin, B.-B. Fu, P. Richard, G.-F. Chen, Z. Fang, X. Dai, H.-M. Weng, T. Qian, H. Ding, and S. H. Pan, Evidence for Topological Edge States in a Large Energy Gap near the Step Edges on the Surface of ZrTe₅, *Phys. Rev. X* **6**, 021017 (2016).
- [9] H. M. Weng, A. Ranjbar, Y. Y. Liang, Z. D. Song, M. Khazaei, S. J. Yunoki, M. Arai, Y. Kawazoe, Z. Fang, and X. Dai, Large-gap two-dimensional topological insulator in oxygen functionalized MXene, *Phys. Rev. B* **92**, 075436 (2015).
- [10] H. J. Zhang, Y. Ma, and Z. F. Chen, Quantum spin Hall insulators in strain-modified arsenene, *Nanoscale* **7**, 19152 (2015).
- [11] Z. F. Wang, N. H. Su, and F. Liu, Prediction of a two-dimensional organic topological insulator, *Nano Lett.* **13**, 2842 (2013).
- [12] L. J. Zhou, L. Z. Kou, Y. Sun, C. Felser, F. M. Hu, G. C. Shan, S. C. Smith, B. H. Yan, and T. Frauenheim, New family of quantum spin Hall insulators in two-dimensional transition-metal halide with large nontrivial band gaps, *Nano Lett.* **15**, 7867 (2015).
- [13] Y. D. Ma, L. Z. Kou, X. Li, Y. Dai, S. C. Smith, and T. Heine, Quantum spin Hall effect and topological phase transition in two-dimensional square transition-metal dichalcogenides, *Phys. Rev. B* **92**, 085427 (2015); Y. D. Ma, L. Z. Kou, X. Li, Y. Dai and T. Heine, Two-dimensional transition metal dichalcogenides with a hexagonal lattice: Room-temperature quantum spin Hall insulators, *ibid.* **93**, 035442 (2016).
- [14] S. M. Nie, Z. Song, H. M. Weng, and Z. Fang, Quantum spin Hall effect in two-dimensional transition-metal dichalcogenide haeckelites, *Phys. Rev. B* **91**, 235434 (2015).
- [15] X. F. Qian, J. W. Liu, L. Fu, and J. Li, Quantum spin Hall effect in two-dimensional transition metal dichalcogenides, *Science* **346**, 1344 (2014).
- [16] F.-C. Chuang, L.-Z. Yao, Z.-Q. Huang, Y.-T. Liu, C.-H. Hsu, T. Das, H. Lin, and A. Bansil, Prediction of large-gap two-dimensional topological insulators consisting of bilayers of group III elements with Bi, *Nano Lett.* **14**, 2505 (2014).
- [17] Z. Y. Zhu, Y. C. Cheng, and U. Schwingenschlögl, Topological Phase Diagrams of Bulk and Monolayer TiS_{2-x}Te_x, *Phys. Rev. Lett.* **110**, 077202 (2013).
- [18] Z. F. Wang, L. Chen, and F. Liu, Tuning topological edge states of Bi(111) bilayer film by edge adsorption, *Nano Lett.* **14**, 2879 (2014).
- [19] W. Luo and H. J. Xiang, Room temperature quantum spin Hall insulators with a buckled square lattice, *Nano Lett.* **15**, 3230 (2015).
- [20] Y. D. Ma, Y. Dai, L. Z. Kou, T. Frauenheim, and T. Heine, Robust two-dimensional topological insulators in methyl-functionalized bismuth, antimony, and lead bilayer films, *Nano Lett.* **15**, 1083 (2015).

- [21] K.-H. Jin and S.-H. Jhi, Quantum anomalous Hall and quantum spin-Hall phases in flattened Bi and Sb bilayers, *Sci. Rep.* **5**, 8426 (2015).
- [22] Z. G. Song, C. C. Liu, J. B. Yang, J. Z. Han, B. T. Fu, M. Ye, Y. C. Yang, Q. Niu, J. Lu, and Y. G. Yao, Quantum spin Hall insulators and quantum valley Hall insulators of BiX/SbX ($X = \text{H, F, Cl}$ and Br) monolayers with a record bulk band gap, *NPG Asia Mater.* **6**, e147 (2014).
- [23] J. J. Zhou, W. X. Feng, C.-C. Liu, S. Guan, and Y. G. Yao, Large-gap quantum spin Hall insulator in single layer bismuth monobromide Bi_4Br_4 , *Nano Lett.* **14**, 4767 (2014).
- [24] H. Weng, X. Dai, and Z. Fang, Transition-metal Pentatelluride ZrTe_5 and HfTe_5 : A Paradigm for Large-Gap Quantum Spin Hall Insulators, *Phys. Rev. X* **4**, 011002 (2014).
- [25] Y. D. Ma, L. Z. Kou, A. J. Du, and T. Heine, Group 14 element-based non-centrosymmetric quantum spin Hall insulators with large bulk gap, *Nano Res.* **8**, 3412 (2015).
- [26] C. Si, J. W. Liu, Y. Xu, J. Wu, B.-L. Gu, and W. H. Duan, Functionalized germanene as a prototype of large-gap two-dimensional topological insulators, *Phys. Rev. B* **89**, 115429 (2014).
- [27] Y. Xu, B. H. Yan, H.-J. Zhang, J. Wang, G. Xu, P. Tang, W. H. Duan, and S.-C. Zhang, Large-Gap Quantum Spin Hall Insulators in Thin Films, *Phys. Rev. Lett.* **111**, 136804 (2013).
- [28] Q. H. Liu, X. W. Zhang, L. B. Abdalla, A. Fazzio, and A. Zunger, Switching a normal insulator into a topological insulator via electric field with application to phosphorene, *Nano Lett.* **15**, 1222 (2015).
- [29] E. O. Wrasse and T. M. Schmidt, Prediction of two-dimensional topological crystalline insulator in PbSe monolayer, *Nano Lett.* **14**, 5717 (2014).
- [30] C. W. Niu, P. M. Buhl, G. Bihlmayer, D. Wortmann, S. Blugel, and Y. Mokrousov, Topological crystalline insulator and quantum anomalous Hall states in IV-VI-based monolayers and their quantum wells, *Phys. Rev. B* **91**, 201401 (2015).
- [31] J. W. Liu, X. F. Qian, and L. Fu, Crystal field effect induced topological crystalline insulators in monolayer IV-VI semiconductors, *Nano Lett.* **15**, 2657 (2015).
- [32] A. L. Araújo, E. O. Wrasse, G. J. Ferreira, and T. M. Schmidt, Topological nonsymmorphic ribbons out of symmorphic bulk, *Phys. Rev. B* **93**, 161101 (2016).
- [33] R. E. Simpson, P. Fons, A. V. Kolobov, T. Fukaya, M. Krbal, T. Yagi, and J. Tominaga, Interfacial phase-change memory, *Nat. Nanotechnol.* **6**, 501 (2011).
- [34] Y. Saito, J. Tominaga, P. Fons, A. Kolobov, and T. Nakano, *Ab-initio* calculations and structural studies of $(\text{SiTe})_2(\text{Sb}_2\text{Te}_3)_n$ ($n: 1, 2, 4$ and 6) phase-change superlattice films, *Phys. Status Solidi RRL* **8**, 302 (2014).
- [35] B. S. Sa, Z. M. Sun, and B. Wu, The development of two dimensional group IV chalcogenides, blocks for van der Waals heterostructures, *Nanoscale* **8**, 1169 (2016).
- [36] S. Keuleyan, M. J. Wang, F. R. Chung, J. Commons, and K. J. Koski, A Silicon-based two-dimensional chalcogenide: Growth of Si_2Te_3 nanoribbons and nanoplates, *Nano Lett.* **15**, 2285 (2015).
- [37] G. Kresse and J. Furthmüller, Efficient iterative schemes for *ab initio* total-energy calculations using a plane-wave basis set, *Phys. Rev. B* **54**, 11169 (1996).
- [38] P. E. Blochl, Projector augmented-wave method, *Phys. Rev. B* **50**, 17953 (1994).
- [39] G. Kresse and D. Joubert, From ultrasoft pseudopotentials to the projector augmented-wave method, *Phys. Rev. B* **59**, 1758 (1999).
- [40] J. P. Perdew, K. Burke, and M. Ernzerhof, Generalized Gradient Approximation Made Simple, *Phys. Rev. Lett.* **77**, 3865 (1996).
- [41] J. Heyd, G. E. Scuseria, and M. Ernzerhof, Hybrid functionals based on a screened Coulomb potential, *J. Chem. Phys.* **118**, 8207 (2013).
- [42] H. J. Monkhorst and J. D. Pack, Special points for Brillouin-zone integrations, *Phys. Rev. B* **13**, 5188 (1976).
- [43] X. Gonze and C. Lee, Dynamical matrices, Born effective charges, dielectric permittivity tensors, and interatomic force constants from density-functional perturbation theory, *Phys. Rev. B* **55**, 10355 (1997).
- [44] A. Togo, F. Oba, and I. Tanaka, First-principles calculations of the ferroelastic transition between rutile-type and CaCl_2 -type SiO_2 at high pressures, *Phys. Rev. B* **78**, 134106 (2008).
- [45] See Supplemental Material at <http://link.aps.org/supplemental/10.1103/PhysRevB.94.201104> for the results of MD simulation at 300 K, parities of the occupied bands, PBE and HSE06 electronic structures of SiTe 2D crystal under various strains, and electronic band structures of GeTe and SnTe 2D crystals.
- [46] V. Nicolosi, M. Chhowalla, M. G. Kanatzidis, M. S. Strano, and J. N. Coleman, Liquid exfoliation of layered materials, *Science* **340**, 1226419 (2013).
- [47] L. Fu, C. L. Kane, and E. J. Mele, Topological Insulators in Three Dimensions, *Phys. Rev. Lett.* **98**, 106803 (2007).
- [48] M. Z. Hasan and C. L. Kane, *Colloquium*: Topological insulators, *Rev. Mod. Phys.* **82**, 3045 (2010).
- [49] W. X. Feng, J. Wen, J. J. Zhou, D. Xiao, and Y. G. Yao, First-principles calculation of Z_2 topological invariants within the FP-LAPW formalism, *Comput. Phys. Commun.* **183**, 1849 (2012).